Measurement of the nuclear enhancement in high-E_t and jet event production

R. Gomez
California Institute of Technology, Pasadena, California 91125

L. Dauwe,[*] H. Haggerty, E. Malamud, and M. Nikolic[†]
Fermilab, Batavia, Illinois 60510

S. Hagopian and A. Pifer[‡]
Florida State University, Tallahassee, Florida 32306

R. Abrams,[§] J. Ares, H. Goldberg, C. Halliwell, S. Margulies, D. McLeod,
A. Salminen, J. Solomon, and G. Wu[**]
University of Illinois at Chicago, Chicago, Illinois 60680

S. Blessing, R. Crittenden, P. Draper,[††] A. Dzierba, R. Heinz, J. Krider,[‡‡]
T. Marshall, J. Martin, A. Sambamurti, P. Smith, A. Snyder, C. Stewart,
T. Sulanke, and A. Zieminski
Indiana University, Bloomington, Indiana 47405

R. Ellsworth
George Mason University, Fairfax, Virginia 22030

J. Goodman, S. Gupta,[§§] and G. Yodh
University of Maryland, College Park, Maryland 20742

T. Watts
Rutgers University, Piscataway, New Jersey 08854

V. Abramov, Yu. Antipov, B. Baldin, S. Denisov, V. Glebov, Y. Gorin,
V. Kryshkin, A. Petrukhin, S. Polovnikov, and R. Sulyaev
Institute for High Energy Physics, Serpukhov, USSR
(Received 1 December 1986)

Properties of events produced with high values of transverse energy (E_t) in 800-GeV/c proton-nucleus collisions are presented. Both full-azimuth and limited-aperture high-E_t triggers were used to select events from six targets (H, Be, C, Al, Cu, and Pb). The events were collected using the large-acceptance Fermilab multiparticle spectrometer that recorded almost 95% of the incoming beam energy. The A dependence of the cross sections at a given E_t was parametrized as A^α. The value of α increases from 0.7 at low E_t to a plateau at high E_t of approximately 1.6. The high-E_t value of α is slightly smaller for the limited-aperture triggers. A strong dependence of α on the event structure is observed; "jetlike" events exhibit an A dependence consistent with $\alpha \approx 1.0$, while for more isotropic events α is much larger. This observation is consistent with the expected behavior for jet production in pA collisions.

I. INTRODUCTION

High-energy collisions of protons with nuclei (pA) have been studied and compared with proton-proton (pp) collisions primarily to measure the effect of interactions of secondaries produced in the initial scatter with other nucleons in the nucleus.[1] These studies have led to a better understanding of the space-time development of the intermediate hadronic matter. Of particular interest are collisions that produce large amounts of transverse energy (E_t) relative to the incident beam direction. Two competing mechanisms are believed to be responsible for such

collisions: (1) multiple soft scattering involving many nucleons within the nucleus and (2) hard scattering of constituents that can produce high-p_t jets which then propagate through the nucleus. Previous experiments[2-8] have found a strong nuclear dependence for the production of high-E_t events. In this paper results are presented from experiment E557/E672 which expand these measurements and further isolate the hard-scattering component by using a higher beam momentum (800-GeV/c protons, pp $\sqrt{s} = 38.8$ GeV) and larger event samples collected with a variety of triggers and targets.

Data from pp and pA high-E_t collisions were taken

TABLE I. Event totals and integrated luminosities.

Target	Thickness (g/cm^2)		Events recorded	Events used	Luminosity (nb^{-1})
Hydrogen		3.24	414×10^3	138×10^3	30.2 ± 1.5
Beryllium	6.93,	10.6	60×10^3	23×10^3	0.119 ± 0.008
Carbon	4.74,	6.66	131×10^3	38×10^3	2.58 ± 0.15
Aluminum	4.01,	14.8	22×10^3	8×10^3	0.063 ± 0.004
Copper	2.2,	5.24	125×10^3	42×10^3	0.240 ± 0.01
Lead	1.27,	2.97	240×10^3	62×10^3	0.108 ± 0.008

with the large-acceptance Fermilab Multiparticle Spectrometer (MPS). Several triggers with different apertures were employed because of their varying efficiencies in collecting hard scatters and because of their various degrees of bias. Large-aperture triggers predominantly select soft collisions whereas small-aperture triggers are more likely to be dominated by hard scatters.[9] The transverse event structure in the central region was used to further enhance the hard-scattering component of the event sample. Transverse event structure was quantified by the planarity variable P (Sec. V). The high-planarity pp events with high E_t in a small aperture predominantly result from hard scattering.[10,11]

In this experiment, energy deposition in the backward, central, and forward rapidity regions was measured. This paper concentrates on results for which particles were produced in the central rapidity region (laboratory pseudorapidities $2.2 \lesssim \eta_{\mathrm{lab}} \lesssim 3.9$ which corresponds to pp center-of-mass pseudorapidities $-0.85 \lesssim \eta^* \lesssim +0.85$, where $\eta^* = -\ln(\tan\frac{1}{2}\theta^*)$, and θ^* is the pp center-of-mass polar angle for massless particles). Cross sections as a function of E_t and planarity for several different targets and trigger apertures are presented. The A dependence of these cross sections (per nucleus) is parametrized in the standard A^α form. The validity of the A^α form for all the cross sections that were measured is discussed; the values of α as a function of E_t, and the variation of α with the planarity variable (which is related to the A dependence of hard scattering in pA interactions) are presented.

This paper is organized as follows. Brief descriptions of the apparatus and the triggers are given in Sec. II. A summary of the data sample and cuts on the data are described in Sec. III. Cross sections as a function of E_t and their A dependence are presented in Sec. IV. The A dependence of the event structure as determined by planarity is given in Sec. V. Conclusions are presented in Sec. VI.

II. APPARATUS

The layout of the Fermilab MPS facility for the E557/E672 run is shown in Fig. 1. The beam consisted of 800-GeV/c protons directly extracted to the Fermilab MT beam line. The beam intensity was typically $(20-80) \times 10^6$ protons per 20-s spill and the spill frequency was one per minute. For pp data the beam was incident on a 45-cm liquid-hydrogen target; for pA data nuclear targets of Be, C, Al, Cu, and Pb replaced the hydrogen target and were constructed of three successive foils thin enough to avoid significant rescattering (see Table I). Targets of different atomic number were periodically changed back and forth to check for systematic differences in the interaction and trigger rates. Multiwire proportional chambers (49 planes of 17 000 wires) and drift chambers (8 planes of 1472 wires) detected charged particles. Charged-particle momenta were measured using a spectrometer magnet that provided a 0.4-GeV/c P_t kick. The proportional chambers and drift chambers were not used in this analysis except in determining the interaction vertex position.

A series of highly segmented calorimeters, denoted by the names wide angle (WAN), insert (INS), forward
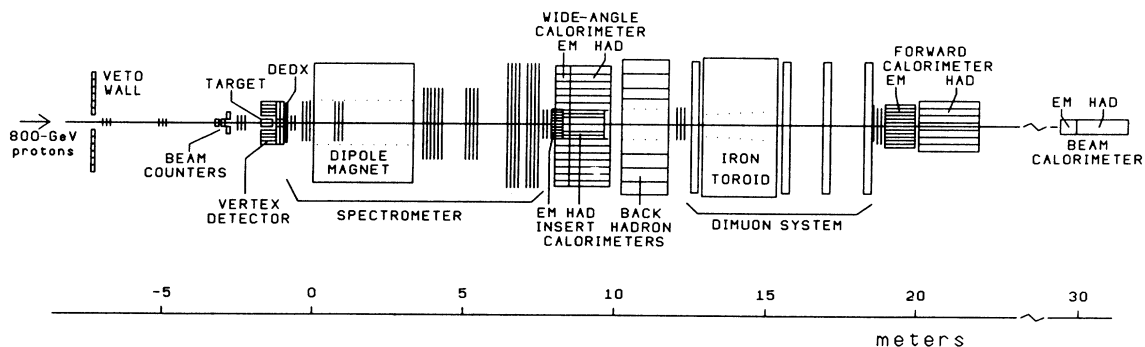

FIG. 1. Apparatus layout for the E557/E672 run.

TABLE II. E557/E672 calorimetry.

Calorimeter type		Material	pp c.m. acceptance		Absorption lengths	Radiation lengths	Resolution coefficient	Number of modules
			$\Delta\theta^*$ (deg)	$\Delta\eta^*$				
WAN	E/M	Pb-scint	145—45	(−1.1)—0.8	0.8	16	0.3	126
WAN	Hadronic	Fe-scint	145—45	−1.1—0.8	3.8	32	0.9	126
BACK	Hadronic	Fe-scint	145—45	−1.1—0.8	3.7	31	0.9	28
INS	E/M	Pb-glass	60—25	0.5—1.5	1.0	16	0.1	84
INS	Hadronic	Fe-scint	60—25	0.5—1.5	5.8	52	0.9	24
FWD	E/M	Pb-glass	30—5	1.3—3.1	1.2	18	0.1	110
FWD	Hadronic	Fe-scint	30—5	1.3—3.1	10	97	1.5	60
BM	E/M	Pb-scint	5—0	>3.1	0.8	15	0.4	1
BM	Hadronic	Fe-scint	5—0	>3.1	10	100	1.5	1
Total			145—0	>-1.1	*	*	*	560

(FWD), and beam (BM), was able to measure 95% of the incident energy. Each of these calorimeters consisted of an electromagnetic section followed immediately downstream by a fully absorptive hadronic section. Parameters for these calorimeters are given in Table II. The WAN calorimeter was used in our previous experiment,[4−6,12] whereas the INS and FWD calorimeters were first used during this run. The geometry and granularity of the WAN, INS, and FWD calorimeters are shown in Fig. 2.

As indicated in Fig. 2 and Table II, the combined geometrical acceptance of the WAN and INS calorimeters was complete in azimuth in the polar angular range $25° \lesssim \theta^* \lesssim 135°$ ($-0.85 \lesssim \eta^* \lesssim +1.5$) as measured in the pp center-of-mass frame for massless particles. In addition to the downstream calorimeters, a vertex detector surrounded the target with 236 proportional tubes and 82 lead-glass modules in order to detect secondaries produced in the target-fragmentation region. Preliminary results from target region data are given in Ref. 13.

Between the WAN and INS calorimeters and the FWD calorimeter was placed a muon detector, consisting of four proportional chambers and a large steel-core toroidal

magnet (see Ref. 14 for details). A hole through the chambers and the toroid of approximately 12 mrad in laboratory polar angle allowed forward-moving particles to reach the FWD and BM calorimeters.

The WAN and INS calorimeters served both as a trigger and a detector of neutral and charged particles. The trigger[15] was based on several conditions.

(i) An inelastic collision was demanded by requiring a beam proton coincident with a pulse height corresponding to four minimum-ionizing particles in a scintillation counter (DEDX) located immediately downstream of the target. This "interacting-beam" (IB) trigger was sensitive to approximately 90% of the total pp inelastic cross section.

(ii) The next requirement was that the incident proton be unaccompanied by another beam particle within ±24 ns. Pulse-height information from a scintillation counter was used to discriminate against beam rf buckets containing more than one particle. In order to prevent event pile up within the 125-ns calorimeter analog-to-digital converter (ADC) integration time, interactions (as defined by DEDX) which occurred within ±150 ns of another in-
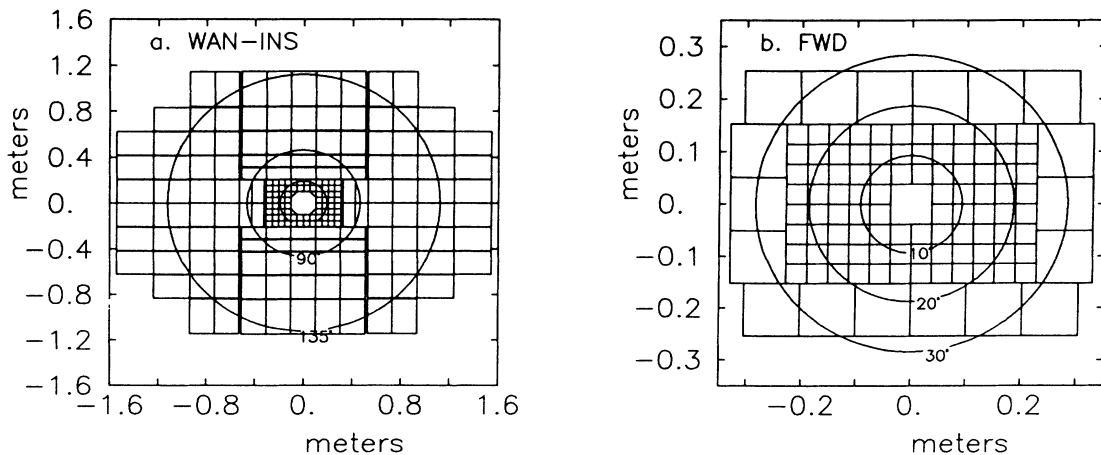

FIG. 2. Calorimeter granularity and center-of-mass angle coverage for massless particles. (a) Wide-angle (WAN) and insert (INS) electromagnetic calorimeters. Circles represent polar angles of 45°, 90°, and 135° in the pp c.m. frame. (b) Forward (FWD) electromagnetic calorimeter. Circles represent polar angles of 10°, 20°, and 30° in the pp c.m. frame.
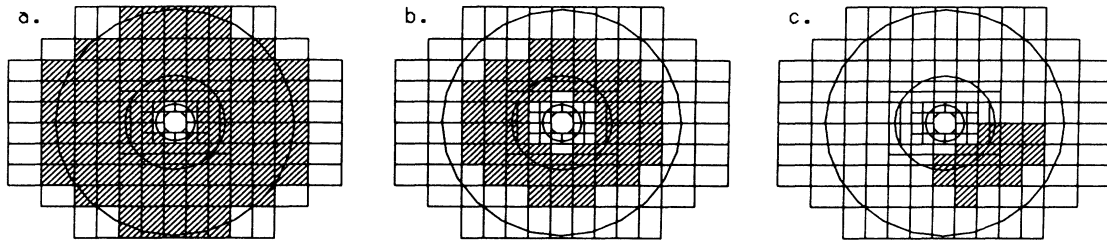
FIG. 3. Trigger apertures in the WAN and INS calorimeters. Circles represent the same polar angles as in Fig. 2(a). (a) Global aperture. (b) Reduced global (RG) aperture. (c) Small aperture (SA). One out of the four SA apertures.

teraction were vetoed.

(iii) The final level of the trigger required that the E_t detected in a section (aperture) of the calorimeter exceed a threshold. Thresholds for different apertures were set independently so that data from 22 different calorimeter trigger apertures could be collected simultaneously. The FWD calorimeter was not used in the triggers discussed here.

The trigger apertures were defined as combinations of the WAN and INS modules divided into four azimuthal sections and four polar-angle sections. Here we present data collected with the following.

(a) The global trigger, which covered the central rapidity region. The global aperture covered the full azimuthal and pp c.m. polar angles $45° < \theta^* < 135°$ $(-0.85 < \eta^* < +0.85)$.

(b) A reduced global (RG) trigger, which was restricted to polar angles $60° < \theta^* < 120°$ $(-0.55 < \eta^* < +0.55)$.

(c) A small-aperture (SA) trigger which covered the same polar region as the RG trigger but only one quarter of the full-azimuthal angle.

Figure 3 shows the geometry of these trigger apertures. Various thresholds for each of the calorimeter triggers were selected so that a wide range of E_t was covered for each target and aperture.

One of the more important details of the apparatus was the energy scale and resolution of the calorimeters. The absolute energy scale of the calorimeter modules was set before data taking in a series of calibration runs with an 80-GeV/c beam. The linearity of the WAN calorimeter response was checked during our previous run.[12] Several INS and FWD moduli were also calibrated with the 800-GeV/c proton beam and these modules were found to be linear with energy. The linearity was also checked for all calorimeters with the laser monitoring system which sent light directly to each module via optic fiber strands.

Each module's resolution was measured during the 80-GeV/c calibration. The responses for the WAN and INS modules, and FWD electromagnetic modules were found to be Gaussian. FWD hadronic modules exhibited a 10% tail due to showers occurring close to the wave shifter bars. Calorimeter module energy resolution is given in
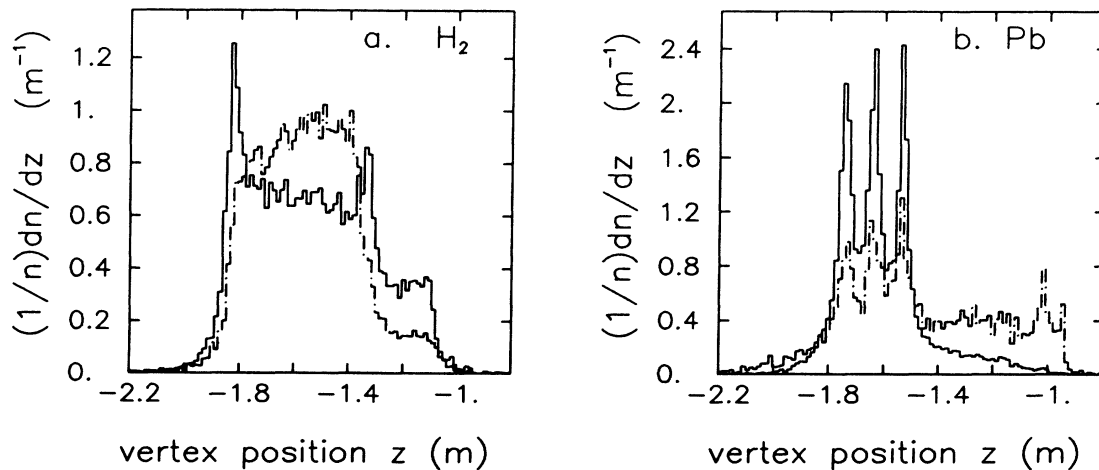

FIG. 4. Vertex distributions for the hydrogen and lead targets. The solid lines are for triggers with high E_t thresholds and the dot-dashed lines are for IB triggers (low E_t). (a) Liquid-hydrogen targets. Events with $-1.8 < z < -1.35$ m survive the vertex cut. (b) Lead target foils. Events with $-1.85 < z < -1.45$ m survive the vertex cut.
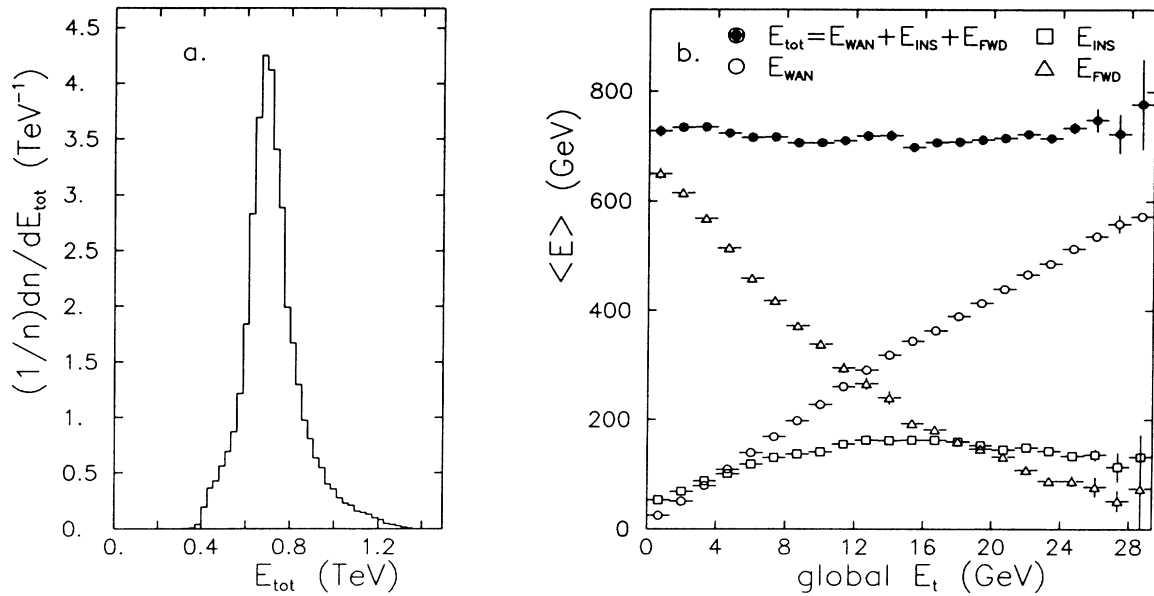
FIG. 5. Total energy measured in the calorimeters. (a) Total-energy (E_{tot}) distribution for pp data. Events with $400 < E_{tot} < 1100$ GeV survive the energy cut. (b) Average E_{tot} vs E_t(global) for pp data. E_t(global) is the transverse energy measured in the global-trigger aperture. Also shown in the plot are the contributions to the total energy of individual calorimeters.

Table II in terms of a resolution coefficient K, where the energy detected in a module has a relative uncertainty of $\sigma(E)/E = K/\sqrt{E}$ (E in GeV). The calibration was re-checked in another series of runs after the data taking was finished. For modules used in the trigger, the shifts in module responses found between the two calibrations were consistent (to within 5%) with shifts determined using the laser monitoring system. The overall shifts were typically less than 10%. The corresponding shifts in module gains (conversion to energy in GeV) used in this analysis were constantly updated by the laser monitoring system.

Another correction to the absolute energy scale was needed because the responses of electromagnetic modules were greater for incident electrons than for hadrons. This "e-π" difference was measured during calibration and was found to be small for the WAN (16%), medium for the INS lead-glass modules (55%), and large for the FWD calorimeter (125%). During our previous run the e-π difference for the WAN calorimeter was measured with a 20-GeV/c beam and was found to be 17% (Ref. 6).

The inherent module energy resolution, calibration uncertainty, energy leakage from modules, the e-π effect (assumed to be energy independent), and the p_t kick of the spectrometer magnet all contributed to an experimental E_t resolution function for each aperture. These effects were simulated using two Monte Carlo models [ISAJET (Ref. 16) and a gluon-bremsstrahlung model[17]] and a calorimeter shower parametrization[18] in order to determine the E_t resolution. The net effect of the E_t resolution on the exponentially falling E_t distributions presented in Sec. IV was a decrease of 17% in the global-aperture E_t scale [E_t(global) is the E_t measured within the global aperture], 16% in the RG aperture E_t scale [E_t(RG) is the E_t measured within the RG aperture], and 8% in the

SA aperture E_t scale [E_t(SA) is the E_t measured within the SA aperture]. The two Monte Carlo models agreed on the size of the E_t shifts. After including this E_t shift, the total uncertainty in the E_t scales was estimated to be 7%. The relative uncertainty of the E_t scales when comparing different nuclear targets is less than 2%.
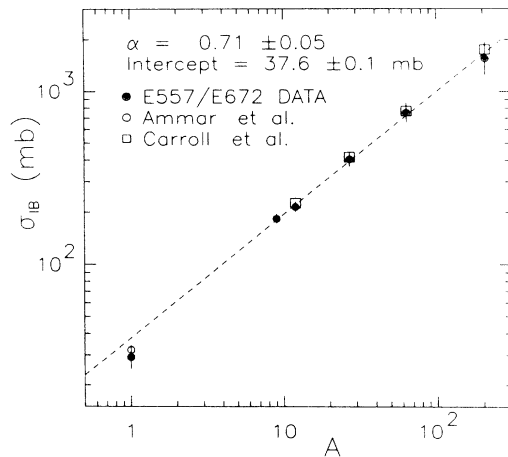

FIG. 6. A dependence for the interacting-beam (IB) cross sections. The dashed line represents a fit to the A^α parametrization (not including hydrogen). Different target thicknesses yielded consistent cross sections and were averaged in this plot. The cross sections here were obtained using the empty target subtraction technique so the points shown were not affected by the vertex-finding inefficiency discussed in the text. Also shown in the plot are data from Refs. 15 and 16.
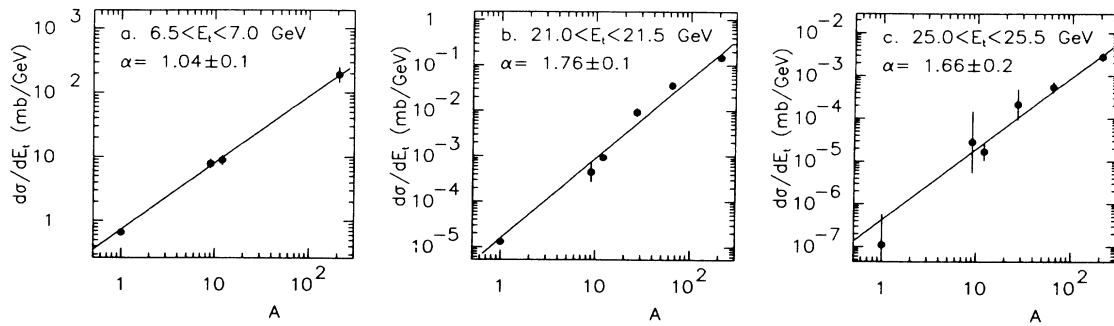
FIG. 7. $d\sigma/dE_t$ cross sections vs A for three sample E_t(global) bins. Solid lines represent fits of the A^α parametrization to the pA data. Hydrogen is not used in the fit. (a) 6.5—7.0 GeV. (b) 21.0—21.5 GeV. (c) 25.0—25.5 GeV.

III. DATA

Table I summarizes the run statistics for all targets and number of events used in this analysis. Data were collected over a one month running period. The sample of events used to measure the cross sections here was selected based on three types of cuts.

(i) A vertex cut discarded events with vertices outside the target volume. Figure 4 shows vertex distributions for the hydrogen target and a lead target for both high-E_t(global) and low-E_t(global) data. In all cases the target outline is clearly identified. For low values of E_t(global), $E_t \lesssim 5$ GeV, half of the interactions in the target were cut due to low charged-multiplicity vertex-finding inefficiencies. The vertex-finding efficiency for events with E_t(global) above 5 GeV increased to 100%. No correction for this vertex-finding inefficiency at low E_t has been made. The peaks at the edges of the hydrogen target (outside of the target volume) for the high-E_t run were due to the enhanced cross section of the target walls, made of Mylar, which have a higher effective A.

(ii) A cut on total energy (E_{tot}) measured in the calorimeters of 400 GeV $< E_{tot} < 1100$ GeV was applied. Figure 5(a) shows the distribution of E_{tot} for pp data. The average E_{tot} is 740 GeV (92% of the energy available from the 800-GeV proton beam) and the full width at half maximum (FWHM) of E_{tot} is equal to 150 GeV when the largest fraction of the total energy is deposited in the WAN calorimeter. The asymmetry in Fig. 5(a) is due to the wave shifter bar problem of the FWD hadronic calorimeter discussed earlier. Since the FWD calorimeter is not included in the trigger the tail has a negligible effect on the data sample. Figure 5(b) shows $\langle E_{tot} \rangle$ as a function of E_t (global). The contributions to $\langle E_{tot} \rangle$ from individual calorimeters are also shown. The dominant contribution from the FWD and BM calorimeters at low E_t (global) became small at high E_t where the WAN calorimeter detected most of the energy. On the average the same amount of total energy was measured irrespective of which of the calorimeters provided most of the energy.

(iii) The final cut required that the observed E_t in a given aperture exceed a predetermined E_t threshold which was slightly greater than the threshold used by the trigger. This cut was designed to eliminate any hardware threshold efficiency effects on the data sample.
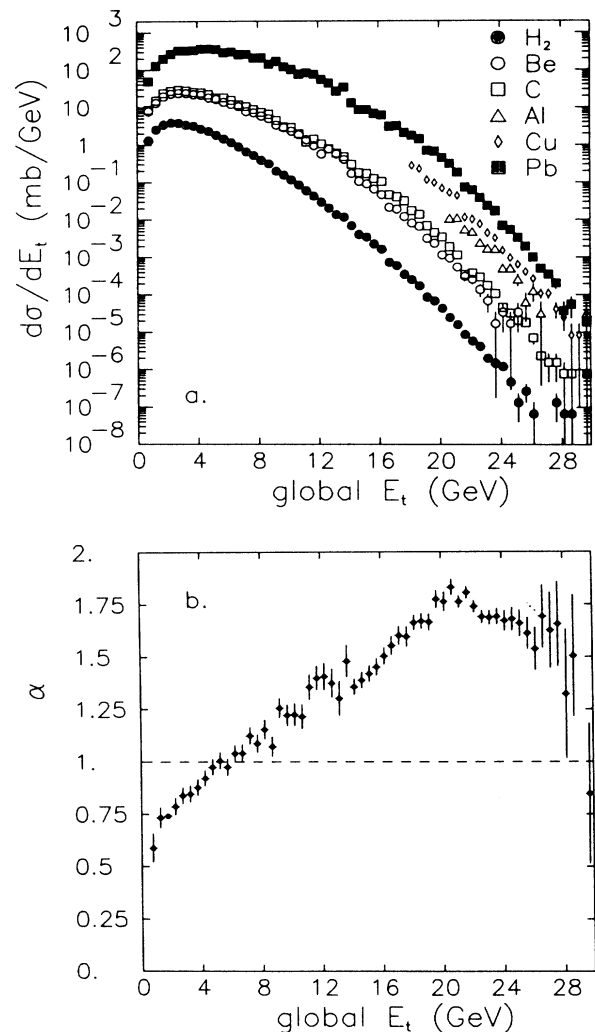

FIG. 8. Global trigger cross sections. The E_t scale in these plots has been corrected 17% for the calorimeter resolution discussed in the text. Error bars are statistical only; run-dependent systematic errors are not included. The data were not corrected for the vertex-finding inefficiency discussed in the text. (a) $d\sigma/dE_t$ vs E_t(global) for all targets. Al and Cu data were taken only at high E_t. (b) α vs E_t(global). Only pA data (not hydrogen) data were used in the A^α fit for this plot and all consequent α vs E_t plots.

After cuts, approximately 30% of the recorded data has been used.

IV. CROSS SECTIONS

The interacting-beam (IB) cross sections were calculated using scaler counts of beam and interactions and corrected for the target thickness. Empty target rates were subtracted directly so no vertex or energy cuts were used to calculate the IB cross section. The pulse threshold of the DEDX counter was set to a signal corresponding to approximately four charged particles. The measured pp IB cross section, 29.1 ± 2 mb, corresponded to 90% of the total inelastic pp cross section, 32.1 ± 0.7 mb (Ref. 19). This difference in cross sections is consistent with bubble-chamber measurements[19] of topological cross sections for two, four, and more charged particles. Figure 6 shows a plot of the IB cross sections as a function of atomic number A. For comparison, values of the total inelastic pA cross sections taken from Refs. 19 and 20 are also shown. The pA data were fitted to a $\sigma_{IB}=\sigma_0 A^{\alpha}$ parametrization. The fit gives $\sigma_0=37.6\pm0.1$ mb and $\alpha=0.71\pm0.05$, in agreement with previous measurements at lower energies.[20]

The $d\sigma/dE_t$ differential cross sections were calculated using events selected by the vertex, E_{tot}, and E_t threshold cuts. Sample $d\sigma/dE_t$ differential cross sections are plotted as a function of A in Fig. 7 for three E_t(global) bins. Data from several high-E_t(global) triggers and the IB trigger were combined to obtain the $d\sigma/dE_t$ cross sections. Figure 7 shows that the A^{α} parametrization is consistent with the data. Values of α at the given E_t(global) bin were the slopes of the $\ln(d\sigma/dE_t)$ vs $\ln(A)$ plots. Hydrogen was not included in the slope calculation. (Hydrogen points usually lay below the pA fitted line so that the value of α would increase slightly if hydrogen were included in the A^{α} fit.)

The $d\sigma/dE_t$ cross sections for the entire range of E_t(global) is shown in Fig. 8(a) for all targets. The integrated pp cross sections from Fig. 8(a) was approximately half of the total IB cross section plotted in Fig. 6. This loss was a result of the 50% vertex-finding efficiency at low E_t discussed in the previous section. Values of $d\sigma/dE_t$ for events with E_t(global) $\gtrsim 5$ GeV show no significant vertex-finding problem due to their higher charged multiplicity at high E_t. Fitted values of α from all E_t bins are plotted vs E_t(global) in Fig. 8(b); $\alpha(E_t)$ rises from 0.7 at low E_t to a plateau value of 1.6 at E_t around 20 GeV.

In comparison with more recent p-Pb data from an experiment described in Ref. 21, the p-Pb $d\sigma/dE_t$ cross section presented in Fig. 8(a) had an extremely low probability (less than 10^{-7}) of exceeding the pp kinematic limit (38.8 GeV). This is due to the difference between the kinematic regions covered by the two experiments. The acceptance of the calorimeter in Ref. 21 covered the backward rapidity region and the p-Pb $d\sigma/dE_T$ cross section presented here covered only the central rapidity region.

Results for the reduced-global (RG) trigger and the small-aperture (SA) trigger are shown in Figs. 9(a) and 10(a). The corresponding α vs E_t(RG) and α vs E_t(SA)

plots show a similar tendency to rise and level off as the global trigger data. In the case of the small-aperture trigger the plateau value of α is significantly lower (by 0.2) than that obtained using the global aperture. This lower value of α may be due to a difference in the processes that dominate the global trigger and the smaller aperture trigger event samples. This possibility is discussed in Sec. V.

The E_t scale correction, determined by Monte Carlo simulation (Sec. III), may *a priori* have had some A dependence due to differences in the event structure for various pA interactions. In order to check this possibility, the energy averaged polar angle in the global aperture, $\langle E_t/E\rangle$, as a function of E_t (global) for several targets was plotted in Fig. 11. At any given value of E_t (global), the energy weighted average polar angle in the global aperture differed by less than 5% when lead events were compared with carbon events. Therefore there was little A dependence of the polar event structure in the central
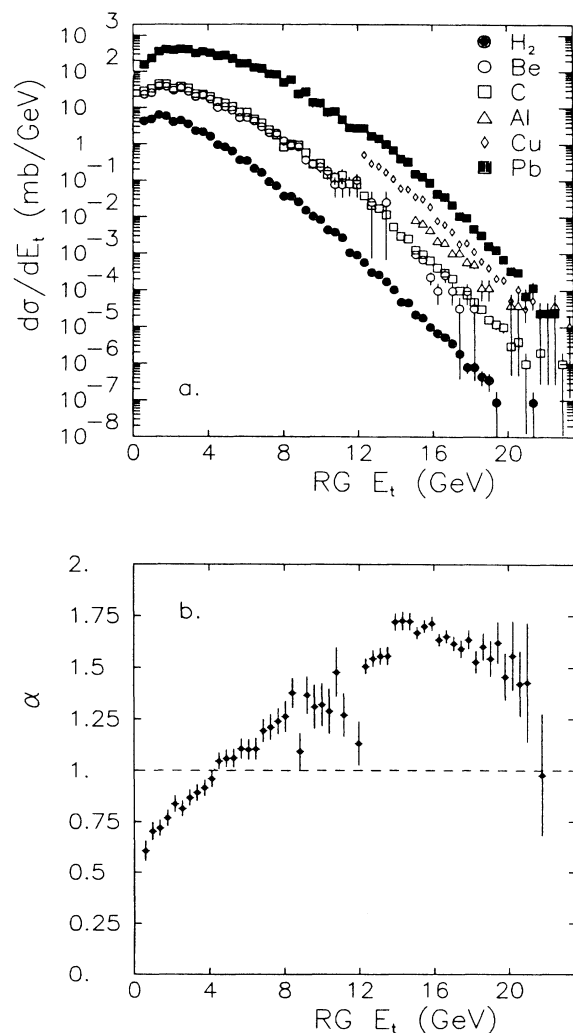

FIG. 9. Reduced-global trigger cross sections. The E_t(RG) scale has been corrected 16% for calorimeter resolution. (a) $d\sigma/dE_t$ vs E_t(RG) for all targets. (b) α vs E_t(RG).

rapidity region. This effect is discussed in more detail in Ref. 13. It is estimated that the small differences in $\langle E_t/E \rangle$ in the nuclear data could result in a systematic shift in α of $+0.05$. Systematic effects of the vertex-finding efficiency on the values of α at low E_t(global) were estimated to be less than ±0.2; the low-E_t values of α were consistent with the interacting beam A dependence with $\alpha \approx 0.7$.

A similar nuclear enhancement of $d\sigma/dE_t$ cross sections at high E_t has been observed in previous experiments.[2-8] These previous measurements have been expanded here to higher energy using improved statistics that have enabled systematic studies of the aperture dependence. Asymptotic values of α at higher E_t presented here (1.4 for SA and 1.6 for global) are somewhat higher than those previously published. The initial rise of

α with E_t is expected from known low-p_t multiplicity distributions for pA collisions.[22] More sophisticated models for soft hadron-nucleus involving multiple collisions have been constructed that successfully agree with $\alpha(E_t)$ data at lower beam energies.[23] These new results for the A dependence of cross sections at high E_t can be used to discriminate between detailed models of hadron-nucleus interactions.

V. EVENT STRUCTURE

The difference in α for high E_t(SA) and high E_t(global) may be due to a difference in the fraction of hard-scatter events and soft-scatter events in the two samples. Transverse event structure in the central region can be used to isolate the "jetlike" events that are expected to arise from a hard-scattering mechanism. Transverse structure is often characterized by the planarity variable[24]

$$P = \max \left[\frac{\sum p_{t\|}^2 - \sum p_{t\perp}^2}{\sum p_{t\|}^2 + \sum p_{t\perp}^2} \right],$$

where $p_{t\perp}$ ($p_{t\|}$) is the perpendicular (parallel) component of a particle's transverse momentum relative to an arbitrary transverse axis.

The axis in the transverse plane is chosen so that P is maximized. Calorimeter module energies and positions are used to calculate p_t; only modules from the global
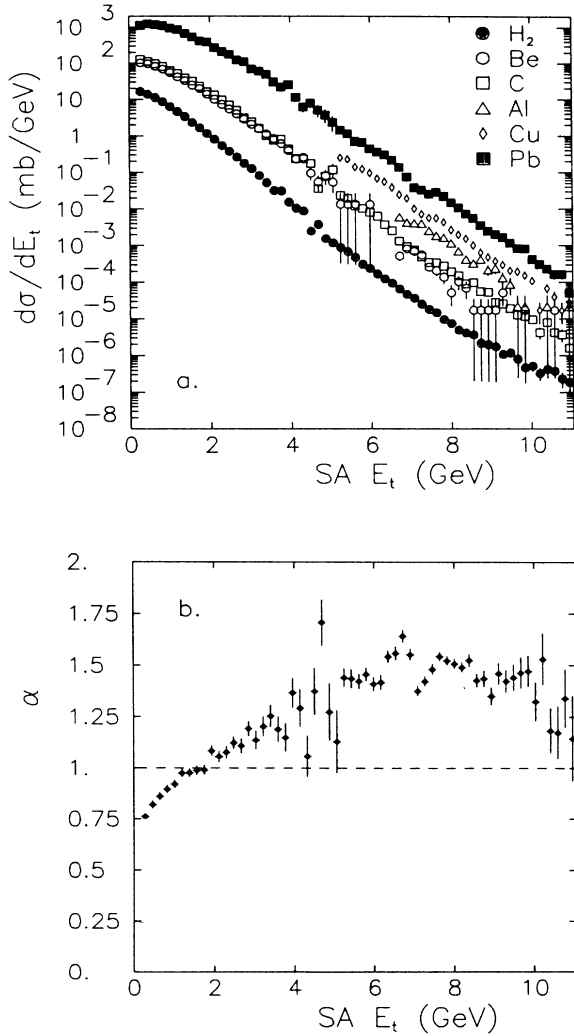

FIG. 10. Small-aperture cross sections. The E_t(SA) scales have been corrected 8% for calorimeter resolution. (a) $d\sigma/dE_t$ vs E_t(SA) for all targets. (b) α vs E_t(SA).

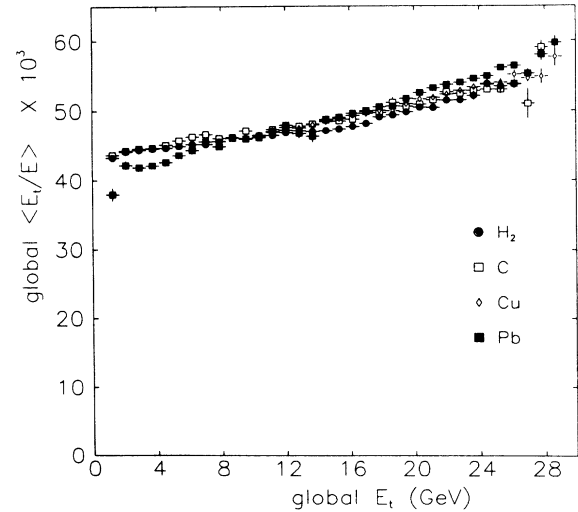

FIG. 11. Average global E_t/E vs E_t(global) for several targets. A dependence in the energy averaged polar angle within the global aperture, $\langle E_t/E \rangle$, could result in an A dependence in the calorimeter E_t resolution. A run-dependent systematic error may have affected the points at low E_t.
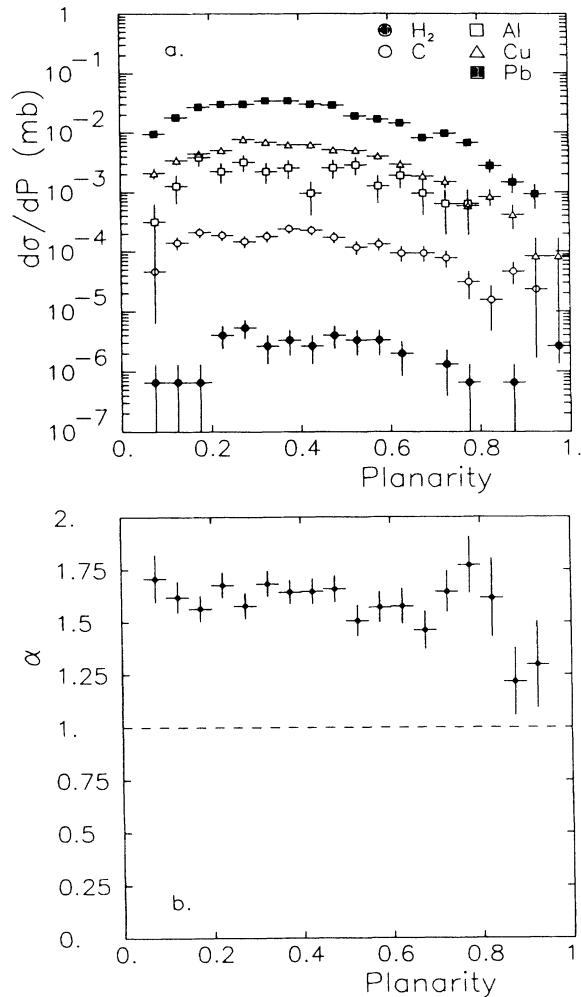
FIG. 12. Global trigger planarity for high-E_t(global) events. Planarity is measured using modules in the global trigger aperture. (a) $d\sigma/dP$ for E_t(global) >23 GeV. Beryllium data is not shown in this plot (as well as the RG and SA plots), due to large statistical errors. (b) α vs P from the global cross sections shown in (a). Be, C, Al, Cu, and Pb data (not hydrogen) were used in the A^α fit.

aperture contributed to the calculation. For back-to-back jetlike structures P approaches one; while for high-multiplicity isotropic event structures P approaches zero. Figure 12(a) shows the planarity distribution for events with E_t (global) greater than 23 GeV. The resulting cross sections in a given planarity range are then plotted against A and the slope, $\alpha(P)$, calculated. As before, hydrogen points were not included. For example, Fig. 13 shows the results of these fits for three bins of planarity for high E_t (SA). The A^α form once again is consistent with the data. As seen from Fig. 12(b), the values of $\alpha(P)$ for events with E_t (global) above 23 GeV are consistent with 1.6 for all planarities.

Cross sections for the reduced-global trigger [E_t(RG) >16 GeV] and the small-aperture trigger [E_t(SA) >8 GeV] as a function of planarity are shown in Figs. 14(a) and 15(a); the corresponding α as a function of planarity is shown in Figs. 14(b) and 15(b). The shapes of the $d\sigma/dP$ cross-section plots obtained using reduced global and small-aperture triggers were strongly dependent on the target; the small-aperture trigger planarity distribution for Pb had an average planarity of $\langle P \rangle = 0.65 \pm 0.02$ and for hydrogen the planarity distribution has $\langle P \rangle = 0.85 \pm 0.02$. Consequently the values of α show a significant drop from 1.6 for $P < 0.7$ to approximately 1.0 ± 0.1 at planarity approaching one. This decrease could be a result of hard scatters dominating the cross section at high planarity with high E_t in a small aperture. Similar values of α have been measured in high-p_t single-particle experiments[25,26] and an A dependence consistent with $\alpha \approx 1.0$ is also seen in Ref. 27 for highly planar events.

Several predictions for the A dependence of hard scattering have been made. Values of α near or slightly above one are expected because the cross section should be proportional to the number of constituents within the nucleus. Corrections due to the structure of the nucleus,[28] Fermi motion,[29] and jet rescattering,[30] increase the predicted value of α for the hard-scattering cross section to 1.1 or 1.2. The result presented here is the most direct indication of the A dependence of a hard-scattering cross section measured in a calorimeter/jet experiment to date.
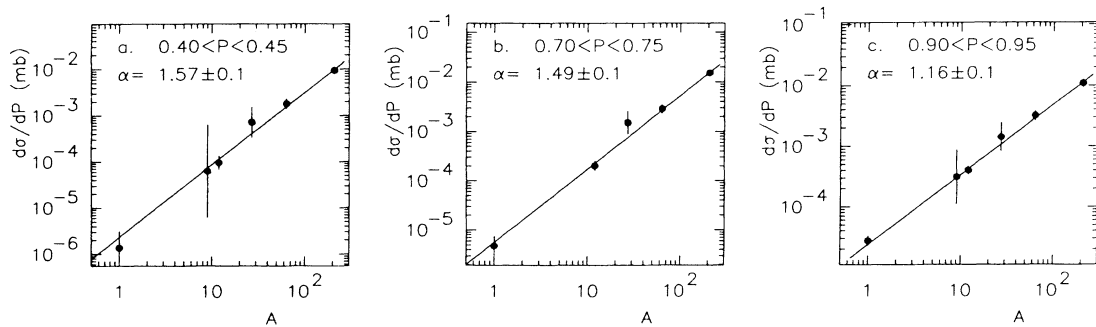

FIG. 13. Three samples of $d\sigma/dP$ differential cross sections vs A for E_t (SA) >8 GeV. Solid lines represent fits to the A^α parametrization. (a) Planarity 0.4—0.45. (b) Planarity 0.7—0.75. (c) Planarity 0.9—0.95.
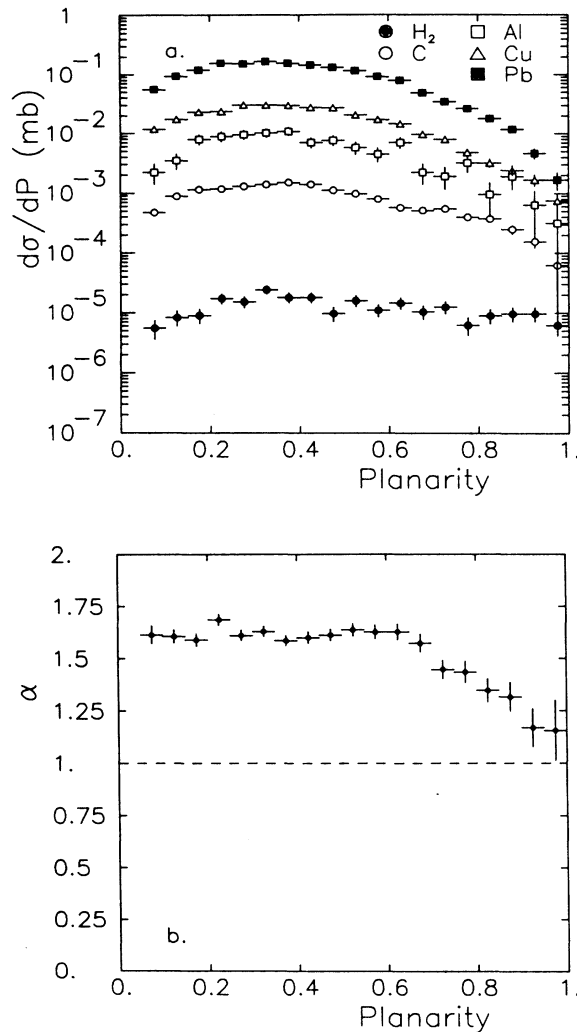
FIG. 14. Reduced-global trigger planarity distributions for high E_t(RG). Planarity is measured using modules in the global trigger aperture. (a) $d\sigma/dP$ at E_t(RG) > 16 GeV. (b) α vs P from the reduced global cross sections shown in (a). Hydrogen data were not used in the A^α fit.

FIG. 15. Small-aperture trigger planarity distributions for high E_t(SA). Planarity is measured using modules in the global-trigger aperture. (a) $d\sigma/dP$ at small aperture E_t(SA) > 8 GeV. (b) α vs P from the small-aperture cross sections shown in (a). Hydrogen data were not used in the A^α fit.

VI. CONCLUSIONS

High-E_t interactions of incident 800-GeV/c protons with nuclear and hydrogen targets were detected by a system of calorimeters that covered $\approx 90\%$ of the c.m. solid angle. The $d\sigma/dE_t$ differential cross sections vs E_t for various triggering apertures and targets have been measured and the nuclear A dependence extracted. The A dependence of the cross sections is described well by the A^α parametrization. Values of α rose from 0.8 at low E_t to 1.6 at high E_t (global) and to 1.4 for high E_t(SA) in a small aperture. In order to enhance the hard-scatter component of the cross section the planarity variable was used to tag jetlike events. The $d\sigma/dP$ differential cross sections for the high-E_t event production have been measured as a function of planarity and their A dependence once again was consistent with the A^α parametrization.
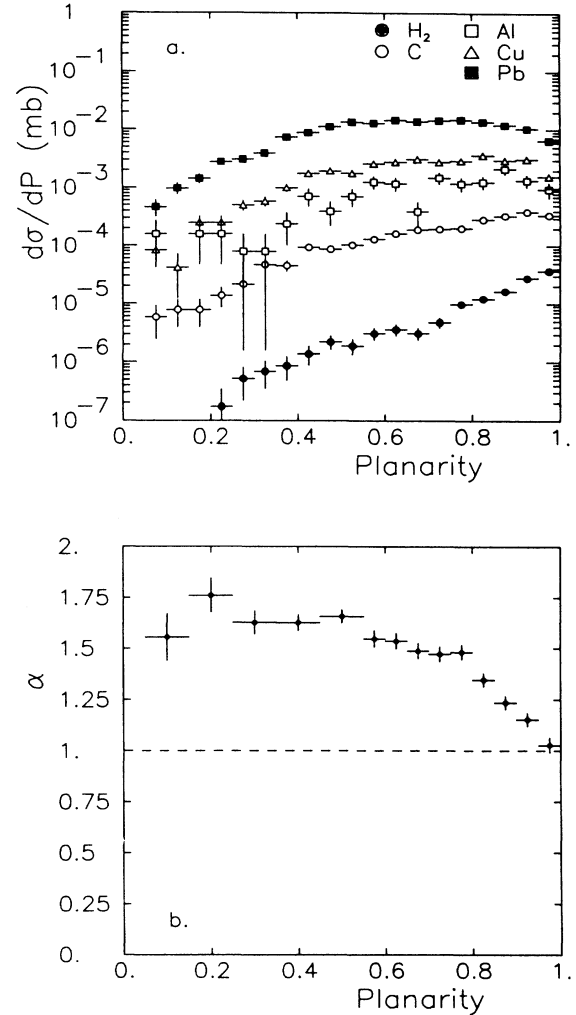
The value of α decreased with increasing planarity for small-aperture triggered events, while for global triggers it did not show a significant dependence on planarity. The value of α for the production of jetlike events approached 1.1 ± 0.1 in agreement with various predictions for the A dependence of hard scattering.

ACKNOWLEDGMENTS

*Present address: Department of Physics, University of Michigan—Flint, Flint, MI 48502.

†Present address: Institute of Nuclear Physics, Novi Sad, Yugoslavia.

‡Present address: Department of Physics, University of Arizona, Tucson, AZ 85721.

§Present address: AT&T Bell Laboratories, Naperville, IL 60540.

**Present address: Department of Physics, Northeastern University, Boston, MA 02115.

††Present address: Department of Physics, University of Rochester, NY 14267.

‡‡Present address: Fermi National Laboratory, Batavia, IL 60510.

§§Present address: Tata Institute of Fundamental Research, Bombay, India 400005.

[1] I. Otterlund, Nucl. Phys. A418, 87 (1984); A. Bialas, in *Proceedings of the Ninth Multiparticle Symposium*, Tábor, Czechoslavakia, 1978, edited by V. Simak, M. Suk, and J. Chyla (Czechoslavakian Academy of Science, Praguel, 1978), and references therein.

[2] C. Bromberg *et al.*, Phys. Rev. Lett. 42, 1202 (1979).

[3] C. Bromberg *et al.*, Nucl. Phys. B171, 38 (1980).

[4] B. Brown *et al.*, Phys. Rev. Lett. 49, 711 (1982).

[5] B. Brown *et al.*, Phys. Rev. Lett. 50, 11 (1983).

[6] B. Brown *et al.*, Phys. Rev. D 29, 1895 (1984).

[7] T. Akesson *et al.*, Phys. Lett. 119B, 464 (1982).

[8] H. Miettinen *et al.*, Nucl. Phys. A418, 315 (1984).

[9] T. Akesson and H. Bengtsson, Phys. Lett. 120B, 233 (1982).

[10] T. Akesson *et al.*, Phys. Lett. 118B, 185 (1982).

[11] L. R. Cormell *et al.*, Phys. Rev. Lett. 53, 1988 (1985).

[12] P. Rapp *et al.*, Nucl. Instrum. Methods 188, 285 (1981).

[13] R. Gomez *et al.*, in *Hadronic Matter in Collision*, proceedings of the 2nd International Workshop on Local Equilibrium in Strong Interaction Physics, Los Alamos, New Mexico, 1986, edited by P. Carruthers and D. Strottman (World Scientific, Singapore, 1986); G. Wu, thesis, Northwestern University, 1986 (unpublished).

[14] R. Crittenden *et al.*, E557/E672 Memo No. 141, 1986 (unpublished).

[15] A. Dzierba *et al.*, E557/E672 Memo No. 142, 1986 (unpublished).

[16] F. Paige and S. Protopopescu, Brookhaven Report No. BNL-38034-mc, 1986 (unpublished).

[17] R. Gomez *et al.*, XXIII International Conference on High Energy Physis, Berkeley California, Abstract No. 1660, 1986 (unpublished).

[18] M. della Negra, Phys. Scr. 23, 465 (1981).

[19] R. Ammar *et al.*, Phys. Lett. 178B, 124 (1986).

[20] A. S. Carroll *et al.*, Phys. Lett. 80B, 319 (1982).

[21] A. Franz *et al.*, Nucl. Phys. A447, 475 (1986).

[22] R. Gomez *et al.*, XXIII International Conference on High Energy Physics, Berkeley, California, Abstract No. 1678, 1986 (unpublished).

[23] H. Brody *et al.*, Phys. Rev. D 28, 2334 (1983).

[24] De Marzo *et al.*, Phys. Lett. 112B, 173 (1982).

[25] J. Cronin *et al.*, Phys. Rev. D 11, 3105 (1975); D. Antreasynan *et al.*, *ibid.* 19, 764 (1979).

[26] J. A. Crittenden *et al.*, Phys. Rev. D 34, 2584 (1986).

[27] Fermilab E609 Collaboration, H. Miettinen (private communication).

[28] A. Krzywicki, Phys. Rev. D 14, 152 (1976).

[29] J. H. Kuhn, Phys. Rev. D 13, 2948 (1976).

[30] U. Sukhatme and G. Wilk, Phys. Rev. D 25, 1978 (1982).